Mid-latitude and equatorial core surface flow variations derived from observatory and satellite magnetic data

G Ropp, Vincent Lesur

submitted to *Geophys. J. Int.*

Mid-latitude and equatorial core surface flow variations derived from observatory and satellite magnetic data

G. Ropp[1], V. Lesur[1]

[1] *Université Paris Cité, Institut de physique du globe de Paris, CNRS, F-75005 Paris, France.*

SUMMARY

A series of models of the Earth magnetic field and core surface flow have been simultaneously and sequentially co-estimated from year 1999 to 2022. The models were derived from magnetic satellite and ground observatory data using a linear Kalman filter approach and prior statistics based on numerical dynamo simulations. The core field and secular variation model components present the same characteristics as the most recent core field models with slightly higher resolution in time. A principal component analysis of the core surface flow series of models shows that the largest flow variations are observed at high latitudes and under the western part of the Pacific Ocean. Filtering out the flow variation periods longer than ∼11.5 years leads to a filtered azimuthal flow that presents ∼7 years periodicities with patterns propagating westward by $\sim 60^o$ longitude per year. These patterns are present mainly at mid- and equatorial latitudes. They are compatible with a perturbation of the main flow made of small columnar flows with rotation axis intersecting the core-mantle boundary between 10^o to 15^o latitudes, and flow speed of less than $5km/y$. Present at all longitudes, these columnar flows are particularly strong under the Pacific Ocean after 2013. They can also be clearly identified under the Atlantic Ocean from 2005 to 2015.

Key words: Core, Core surface flow, Magnetic field model, Satellite magnetics, Magnetic field variations through time.

1 INTRODUCTION

The Earth's geomagnetic field has been known to vary with time for centuries and to monitor these variations magnetic observatories were established from the middle of the 19th century (Gauss & Weber 1839). At the observatory sites the Earth's core field slow variation (the secular variation) is recorded continuously. It presents sudden changes of slope, that have been described as "geomagnetic jerks" (Courtillot et al. 1978). This view of a relatively slow evolution of the magnetic field in between "jerks" (Courtillot & Le Mouël 1988) has been challenged in the first decade of the 21st century: the analysis of accumulated satellite data allowed the magnetic field acceleration (i.e. second time derivative) to be modelled giving evidence of recurrent fast core magnetic field variations (Olsen & Mandea 2008; Lesur et al. 2008). These fast variations were observed mainly in the African hemisphere (i.e. under the Indian Ocean, Africa and the Atlantic Ocean), or at high latitudes. However, the succession of magnetic satellite missions have shown that fast variations also occurred under the Pacific Ocean (i.e. the Pacific hemisphere) between 2015 and 2018 (Finlay et al. 2020). It is not yet clear if these latter variations form an isolated event or, to the contrary, if it is the absence of fast variations in the Pacific hemisphere over the first decade of the 21st century that is an exception.

The observed fast variations raise questions on the dynamics of the Earth's core flow that generate them. Yet the information on the flow derived from magnetic observations is partial, limited to large scales and, regarding the temporal evolution of the flow, particularly difficult to extract. Models of the core magnetic field and its secular variation allow models of the core surface flow at the core-mantle boundary, just below the liquid viscous boundary layer at the top of the free stream, to be derived. This step relies on the radial component of the induction equation as it was proposed by Roberts & Scott (1965). Most of the derived models show that the core surface flow is dominated by a large scale quasi-geostrophic gyre flowing westward close to the inner-core tangent cylinder in the Pacific hemisphere, and at the core mantle boundary in the African hemisphere (Pais & Jault 2008). However there are still large uncertainties regarding smaller scales and their evolution with time. This comes from the large number of parameters required to describe the flow, much larger than the

number of parameters resolved from our partial knowledge of the core magnetic field and its secular variation at the Earth surface (Holme 2015). To circumvent this difficulty constraints have to be set on the characteristics of the surface flow. Typical examples are to impose a large scale flow (e.g. Bloxham 1988), a purely toroidal flow (e.g. Whaler 1980; Bloxham 1990), tangential geostrophy (e.g. Le Mouël et al. 1985), radial vorticity (e.g. Asari & Lesur 2011), or quasi-geostrophy (e.g. Pais & Jault 2008; Gillet et al. 2009). There are other difficulties to handle such as the contribution of the small scale core field and flow to the large scale secular variation (Eymin & Hulot 2005). As models of the core field and secular variation improved over the last two decades, this latter issue has attracted more attention. It is generally handled by adjusting the error budget of the secular variation model (e.g. Pais & Jault 2008; Baerenzung et al. 2014; Lesur et al. 2015), but the contribution of the small scale core field and flow has also been co-estimated with the large scale flow (e.g. Barrois et al. 2017, 2018). The secular variation, as the core field, are however subject to modelling errors that are difficult to estimate. It is nonetheless important to account for these errors to assess if a particular flow structure evolving in time is robust or not. The flow model errors are rarely provided (see Baerenzung et al. 2014, 2016; Baerenzung et al. 2018, for a few examples).

Recent numerical simulations of the Earth's dynamo (Aubert & Gillet 2021) suggest that the observed large scale gyre is essentially steady on a time scale of a few decades and that it cannot explain the observed fast variations of the magnetic field. There is converging evidence that on shorttime-scales, torsional waves with a period close to 5 years propagating radially away from the Earth's rotation axis at the Alfven speed are present in the core (Gillet et al. 2010). It should be noted that these waves represent only a small fraction of the flow total energy. They have not yet been clearly identified in core flow models derived from satellite based field models. More recently Magneto-Coriolis (MC) eigenmodes have been identified that have a much stronger signature than the torsional waves, and periods about seven years (Gerick et al. 2021; Gillet et al. 2022). An overview of recent progress in modelling magnetic field fast variations and associated rapid dynamics in the core that could explain them is given by Lesur et al. (2022).

In this paper are presented results of core flow modelling where the flow is co-estimated with the core field model and its secular variation as in Lesur et al. (2010, 2015). This carries the advantage that the full error statistics for the core and secular variation are accounted for. An iterative approach based on a linear Kalman filter is used as opposed to most previous

work using ensemble (i.e. nonlinear) filters (Beggan & Whaler 2009; Baerenzung et al. 2018; Barrois et al. 2018; Gillet et al. 2019). The way the core field and flow modelling has been implemented here differs from previous co-estimation work in that neither the field, nor the flow are described in time using B-splines. Rather they are described through a series of snapshot models in the same way that it was implemented by Ropp et al. (2020) for the core field. This carries the advantage that we can reduce the non-linearity of the induction equation. All model parameters are assumed to follow a Gaussian distribution characterised by a mean and a variance (see e.g. Holschneider et al. 2016). As priors we rely on the outputs of numerical dynamo simulations. We used the Coupled-Earth (CE) dynamo model (Aubert et al. 2013).

As a result of our modelling work we obtained a precise description of the core magnetic field from 1999 to 2022, together with a model of the core flow. Although numerous aspects of the magnetic field and flow model evolution are interesting, we focus here on the analysis of the mid-latitude and equatorial flows and their temporal variations. In the next section we describe the data sets we used: satellite and ground observatory data. Then we describe in sections 3 and 4 the model parameterisation and the modelling method. Results are presented in section 5, and discussed in section 6. We conclude in section 7

2 DATA

The work presented here is based on satellite and ground observatory data from 1999.0 to 2022.0. These include vector data from the Danish Oersted satellite, the German CHAMP satellite, and the ESA CryoSat-2 and Swarm satellite missions. For Oersted and CHAMP the last version of calibrated data are used, whereas for CryoSat-2 we used the version calibrated by Olsen et al. (2020). For the Swarm mission, the data version 0506 or 0601 is used depending on availability, exclusively from the Swarm–A satellite. Regarding observatory data we rely on the data set made available by Macmillan & Olsen (2013) as distributed on the 21/11/2021.

The data have been selected using similar criteria as Ropp et al. (2020) to limit contributions from the ionosphere and magnetosphere systems of currents, as well as their counterpart induced currents in the conductive layers of the Earth (Thomson & Lesur 2007). This selection is based on the data local-time, whether the ionosphere is sun lit or not, the interplanetary magnetic field (IMF) direction, the D_{st} index, and includes dependence on whether the data magnetic latitude is inside or outside the $\pm 55^o$ interval (see table 1). As our target contribution is the core field, there is no need to have a high density of sampling points along a satellite

Data type	Oersted		Champ		CryoSat		Swarm		Obs	
Dates	[1999.2 : 2004.0]		[2000.5 : 2010.7]		[2010.6 : 2014.0]		[2013.9 : 2022.0]		[1999.0 : 2021.8]	
$\lvert\text{Lat}_m\rvert$	$\geq 55^o$	$< 55^o$	$\geq 55^o$	$< 55^o$	$\geq 55^o$	$< 55^o$	$\geq 55^o$	$< 55^o$	$\geq 55^o$	$< 55^o$
Coor. Sys.	NEC	SM	NEC	SM	NEC	SM	NEC	SM	NEC	SM
Selection criteria										
LT (h)	all	[23:05]	all	[23:05]	all	[23:05]	all	[23:05]	all	[23:05]
Sampling	60s	20s	60s	20s	60s	30s	60s	30s	1h	1h
Sun lit Io.	yes	no	yes	no	yes	no	yes	no	no	no
D_{st} (nT)	± 30	± 30	± 30	± 30	± 30	± 30	± 30	± 30	± 30	± 30
$\partial_t D_{st}$ ($\frac{\text{nT}}{day}$)	± 100	± 100	± 100	± 100	± 100	± 100	± 100	± 100	± 100	± 100
IMF B_z	> 0	> 0	> 0	> 0	> 0	> 0	> 0	> 0	> 0	> 0
Nb. data	244797	325972	649562	1013919	300666	219713	728968	545888	1101750	1954148
Prior standard deviation (σ^p)										
X	10 nT	4.2 nT	10 nT	3 nT	10 nT	3 nT	10 nT	3 nT	6 nT	4 nT
Y	9 nT	4.2 nT	9 nT	3 nT	9 nT	3 nT	9 nT	3 nT	5 nT	4 nT
Z	9 nT	5.7 nT	9 nT	4 nT	9 nT	4 nT	9 nT	4 nT	6 nT	5 nT

Table 1. Data selection criteria and prior standard deviations σ^p, both depending on magnetic data type. Lat_m is the magnetic latitude. LT is the local time, given as intervals in hours. SM stands for solar-magnetic system of coordinate, and NEC is the usual North, East, Centre spherical coordinate system.

orbit. We therefore sub-sample satellite data to reduce possible correlated errors between data points. We also subtracted a model of the lithospheric field (Lesur et al. 2013) from spherical harmonic degrees 30 to 110. We did not use total intensity data.

For the least-squares process described below, it is necessary to evaluate as realistically as possible the data errors. Orientation and calibration processes (Tøffner-Clausen et al. 2016) may generate errors that are correlated in space and, as the calibration parameters are smoothed along the satellite trajectory, in time. Similarly the limited resolution of the magnetosphere contributions to the observations generates correlated errors in space and time in our data. We rotate vector data in Solar-Magnetic (SM) coordinate system at mid- and low-latitudes to limit these error correlations between vector components. However in this work the calibration parameters are not co-estimated, and data correlated errors are ignored. This is clearly a limitation we should try to overcome. The prior standard deviations σ^p of the data errors used in the modelling process are given in table 1. They are essentially the same as those used

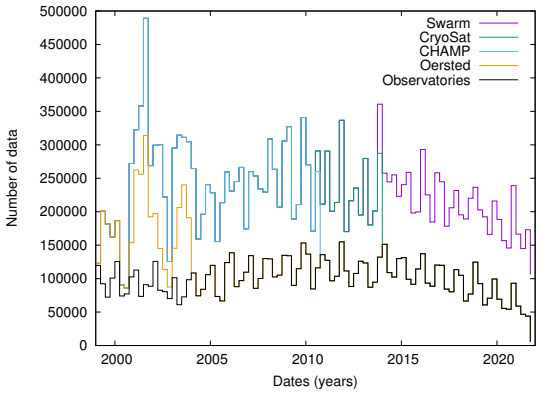

Figure 1. Number of data for ∼3 month steps, with their division into observatory data, and Oersted, CHAMP, CryoSat-2 or Swarm-A satellite data.

by Ropp et al. (2020).

The number of used data, as a function of time and origin, is shown in Figure (1). It should be noted that gross outliers are automatically rejected by our modelling process. They are identified as lying more than five sigma away from the predicted model output for a given time and location. Furthermore, Huber weights are used in our modelling process such that the tails of the data error distribution do not affect significantly the output of our modelling.

3 MODEL PARAMETERISATION

The part of the model dedicated to the description of the geomagnetic field at the Earth's surface is parametrised as described by Ropp et al. (2020). We have added in this work the parameterisation of the core flow at the core mantle boundary. Our modelling process generates a series of snapshot distributions of models. Each distribution is assumed to be Gaussian and is therefore characterised by a mean model (hereinafter referred to as a model) and a covariance matrix. A snapshot model describes the geomagnetic field and core surface flow over three months. This short time-span was chosen to maintain a good balance between robustness and resolution of the derive models, while having a relatively simple snapshot model description.

The magnetic field part of the model includes a description of the core field and a linear secular variation in time up to spherical harmonic degree 18. The lithosphere is modelled from spherical harmonic degree 15 up to 30, but we recall that a reference model of the lithosphere as been subtracted from the data up to spherical harmonic degree 110. There is no description of the

fields generated in the oceans, or in the E-layer of the ionosphere, nor of the toroidal fields generated by field aligned currents. We described the close and far magnetosphere contributions using static field components in SM and GSM systems of coordinates as proposed by Lühr & Maus (2010), although we used here degree 3 maximum spherical harmonics. Magnetospheric field fast variations and their induced counterparts are parameterised through the E_{st} and I_{st} indices respectively, both derived from the D_{st} index as proposed by Maus & Weidelt (2004). Although in principle these indices are set for spherical harmonic degree 1 only we use them up to degree 3. There is also a known dependence of the magnetic data with regard to the IMF B_y component (Lesur et al. 2005). Here it is again parameterised up to spherical harmonic degree 3. As in Ropp et al. (2020), we introduced a field component of internal origin with a linear temporal variation, different from the core or lithosphere, up to spherical harmonic degree 6. We assume this contribution is induced in the mantle or lithosphere from external field variations but it may originate from other processes. By introducing this internal field component in our model, we reduce spurious annual variations that otherwise contaminate the core field model. Finally, the local lithospheric field contributing to observatory data has to be handled. For this purpose three observatory offsets, one for each component, are modelled for each observatory.

Equation (3.1) links the defined set of parameters over a time interval $[t_k, t_{k+1}[$ to the observed magnetic field $\mathbf{B}(r, \theta, \phi, t)$, where r, θ, ϕ, t stand for radius, colatitude, longitude and time ($t = t_k + \delta t$; $\delta t < (t_{k+1} - t_k)$), respectively:

$$
\begin{aligned}
\mathbf{B}(r,\theta,\varphi,t) = & \sum_{\ell,m} \left(\frac{c}{r}\right)^{\ell+2} \left[{}^{\mathrm{C}}g^m_{\ell k} + \delta t \; {}^{\mathrm{C}}\dot{g}^m_{\ell k} \right] \hat{\mathbf{Y}}^m_{\ell,\ell+1}(\theta,\varphi) \\
& + \sum_{\ell,m} \left(\frac{a}{r}\right)^{\ell+2} \left[{}^{\mathrm{L}}g^m_{\ell k} \right] \hat{\mathbf{Y}}^m_{\ell,\ell+1}(\theta,\varphi) \\
& + \sum_{\ell,m} \left(\frac{a}{r}\right)^{\ell+2} \left[{}^{\mathrm{I}}g^m_{\ell k} + \delta t \; {}^{\mathrm{I}}\dot{g}^m_{\ell k} \right] \hat{\mathbf{Y}}^m_{\ell,\ell+1}(\theta,\varphi) \\
& + \sum_{\ell,m} \left(\frac{a}{r}\right)^{\ell+2} \left[{}^{\mathrm{I}st}g^m_{\ell k} \; I_{st}(t) \right] \hat{\mathbf{Y}}^m_{\ell,\ell+1}(\theta,\varphi) \\
& + \sum_{\ell,m} \left(\frac{r}{a}\right)^{\ell-1} \left[{}^{\mathrm{G}}q^m_{\ell k} \right] \hat{\mathbf{Y}}^m_{\ell,\ell-1}(\theta_{GSM},\varphi_{GSM}) \\
& + \sum_{\ell,m} \left(\frac{r}{a}\right)^{\ell-1} \left[{}^{\mathrm{S}}q^m_{\ell k} + {}^{\mathrm{I}}q^m_{\ell k} \; B_y^{\mathrm{IMF}}(t) + {}^{\mathrm{E}st}q^m_{\ell k} \; E_{st}(t) \right] \hat{\mathbf{Y}}^m_{\ell,\ell-1}(\theta_{SM},\varphi_{SM}) \\
& + \sum_i \delta(r - r_i, \theta - \theta_i, \varphi - \varphi_i) \, \mathbf{O}_i + \mathbf{e}_o \; ,
\end{aligned}
\tag{3.1}
$$

where the $g_{\ell k}^m$ and $q_{\ell k}^m$ are the model parameters for internal and external sources, respectively. Prefixes of spherical harmonic coefficients are associated with the source modelled – e.g. $^{\rm C}$ for the core, $^{\rm L}$ for the lithosphere (see table 2 for the list of coefficients associated with each source). The $\mathbf{O}_i$ are the observatory offsets and $(r_i, \theta_i, \varphi_i)$ is the position of the observatory of index i. The vector $\mathbf{e}_o$ is the error in the equation due to the noise in the data and the contributions of un-modelled sources. The $(\theta_{SM}, \varphi_{SM})$ (resp. $(\theta_{GSM}, \varphi_{GSM})$) are the coordinates in SM (resp. GSM) system of coordinates. $a = 6371.2$km and $c = 3485$km are the reference radii for the Earth's surface and core respectively. The $\hat{\mathbf{Y}}_{\ell,\ell'}^m(\theta, \varphi)$ are vector spherical harmonics normalised in the same way as in Lesur & Vervelidou (2020); Ropp et al. (2020) – see Appendix A.

The core surface flow $\mathbf{U}_h$ is decomposed in toroidal and poloidal components (e.g. Holme 2007), each described through spherical harmonics up to degree 26:

$$\mathbf{U}_h(\theta, \varphi) = \sum_{\ell,m} \{ \, [t_\ell^m] \, \nabla_h \times (\hat{\mathbf{r}} Y_\ell^m(\theta, \varphi)) + [s_\ell^m] \, \nabla_h Y_\ell^m(\theta, \varphi) \, \}, \tag{3.2}$$

where t_ℓ^m, s_ℓ^m are the toroidal and poloidal coefficients respectively and ∇_h is the horizontal gradient operator on the unit sphere. $Y_\ell^m(\theta, \varphi)$ are the usual Schmidt-normalised spherical harmonics. There is no time dependence of the core flow over the 3-month span of a snapshot model. To model the core surface flow, we used the radial component of the induction equation:

$$\partial_t B_r = -\frac{1}{c} \nabla_h \cdot (\mathbf{U}_h \, B_r) + D_r, \tag{3.3}$$

where $D_r = \eta \, \mathbf{e}_r \cdot \nabla^2 \mathbf{B}$ is the radial diffusion contribution to the secular variation (η being the magnetic diffusivity and $\mathbf{e}_r$ a radial unitary vector). The discretised form of this equation for the time interval $[t_k, t_{k+1}[$ is:

$$\begin{aligned} 0 = & \frac{4\pi c(\ell+1)}{2\ell+1} \, [{}^{\rm C}\dot{g}_{\ell k}^m] \\ & - \sum_{\ell',m'} \{ \sum_{\ell'',m''} \frac{\ell''+1}{2} \, G_{\ell'',m'',\ell',m'}^{\ell,m} (\ell''(\ell''+1) + \ell'(\ell'+1) - \ell(\ell+1)) \, {}^{\rm C}g_{\ell'' k}^{m''} \, \} \, [s_{\ell' k}^{m'}] \\ & - \sum_{\ell',m'} \{ \sum_{\ell'',m''} (\ell''+1) E_{\ell'',m'',\ell',m'}^{\ell,m} \, {}^{\rm C}g_{\ell'' k}^{m''} \, \} \, [t_{\ell' k}^{m'}] - \frac{4\pi c(\ell+1)}{2\ell+1} \, ([d_{\ell k}^m] + [e_{\ell k}^m]) + e_f \end{aligned} \tag{3.4}$$

where ${}^{\rm C}\dot{g}_{\ell k}^m$ are the Gauss coefficients for the secular variation at the core mantle boundary, and $d_{\ell k}^m$ those of the diffusion contribution to the secular variation. We also introduced truncation error parameters noted $e_{\ell k}^m$. They account for this part of the secular variation due to small scale core field and core flow not resolved in our model. The error term e_f accounts for potential numerical approximations. $G_{\ell'',m'',\ell',m'}^{\ell,m}$ and $E_{\ell'',m'',\ell',m'}^{\ell,m}$ are the Gauss and Elsasser's integrals (Gibson & Roberts 1969). These equations have the maximum degree

$\ell_{max} = \ell''_{max} = 13$ for the secular variation, the core field, the diffusion contribution and the truncation errors, and $\ell'_{max} = 26$ for the poloidal and toroidal flows.

Together, equations (3.1) and (3.4) form the set of equations that are fitted to the magnetic data by adjusting the values of the model parameters – i.e. the various $g^m_{\ell k}$, $\dot{g}^m_{\ell k}$, $q^m_{\ell k}$, the $t^m_{\ell k}$, $s^m_{\ell k}$, $d^m_{\ell k}$, $e^m_{\ell k}$ and $\mathbf{O}_i$ (see table 2). The Gauss coefficients for the static core field ${}^{\mathrm{C}}g^{m''}_{\ell'' k}$ are unknown parameters in equations (3.1). In equations (3.4), they contribute to the terms in curled brackets but are treated as known values. Therefore, only the secular variation Gauss coefficients ${}^{\mathrm{C}}\dot{g}^m_{\ell k}$ link the two sets of equations (3.1) and (3.4) where they are treated as unknown parameters. Of course we could have replaced the ${}^{\mathrm{C}}\dot{g}^m_{\ell k}$ in equations (3.1) by an expression derived from equations (3.4), but we made the choice to model explicitly the secular variation to monitor the sequential process that is described in the next section. The choice of having the ${}^{\mathrm{C}}g^{m''}_{\ell'' k}$ assumed known in equations (3.4) has a second consequence: it reduces the non-linearity of the inverse problem.

To write the equations (3.1) and (3.4) as a linear system of equations, the vector $\mathbf{m_k}$ is defined that contains all 4103 parameters presented in table 2, for the time interval $[t_k, t_{k+1}[$. A matrix $\mathbf{H}$ can be defined such that the equations (3.1) become:

$$\mathbf{d_{Bk}} = \mathbf{H} \cdot \mathbf{m_k} + \mathbf{e_b}, \tag{3.5}$$

where $\mathbf{d_{Bk}}$ contains all vector magnetic data values for this time interval and $\mathbf{e_b}$ their associated errors $\mathbf{e}_o$. Similarly the equations (3.4) write:

$$\mathbf{d_0} = \mathbf{H}_{{}^{\mathrm{C}}\mathbf{g}^{\mathbf{m}}_{\ell \mathbf{k}}} \cdot \mathbf{m_k} + \mathbf{e_f}, \tag{3.6}$$

where $\mathbf{d_0}$ is a null vector with dimension $\ell_{max} \times (\ell_{max} + 2) = 195$ ($\ell_{max} = 13$ is the maximum degree of the secular variation used in equations (3.4)) and $\mathbf{e_f}$ contains the errors e_f. The matrix $\mathbf{H}_{{}^{\mathrm{C}}\mathbf{g}^{\mathbf{m}}_{\ell \mathbf{k}}}$ is built assuming the ${}^{\mathrm{C}}g^m_{\ell k}$ are known. The two linear systems (3.5, 3.6) can be combined in one single system:

$$\mathbf{d_k} = \begin{bmatrix} \mathbf{d_{Bk}} \\ \mathbf{d_0} \end{bmatrix} = \begin{bmatrix} \mathbf{H} \\ \mathbf{H}_{{}^{\mathrm{C}}\mathbf{g}^{\mathbf{m}}_{\ell \mathbf{k}}} \end{bmatrix} \cdot \mathbf{m_k} + \begin{bmatrix} \mathbf{e_b} \\ \mathbf{e_f} \end{bmatrix} = \mathbf{A_k} \cdot \mathbf{m_k} + \mathbf{e_k} \ . \tag{3.7}$$

In section 4 is described how this linear system, valid for the time interval $[t_k, t_{k+1}[$, is solved.

Finally, it should be noted that the diffusion and the truncation errors are explicitly modelled (see equation (3.4)) contrary to what was done in Lesur et al. (2010, 2015) where these

[h]

Source	L_{min}:L_{max}	**Time scale**	**Prior**	**Parameters**
Static core field	1:18	CE model	CE model	${}^{\mathrm{C}}g_{\ell k}^{m}$
Core SV	1:18	11 yr	CE model	${}^{\mathrm{C}}\dot{g}_{\ell k}^{m}$
Toroidal Flow	1:26	30 yr	CE model	$t_{\ell k}^{m}$
Poloidal Flow	1:26	30 yr	CE model	$s_{\ell k}^{m}$
Diffusion term	1:13	$415/\ell$ yr	CE model	$d_{\ell k}^{m}$
Trunc. Errors	1:13	11 yr	CE model	$e_{\ell k}^{m}$
Lithospheric field	15:30	10^6 yr	$R = 6280.\mathrm{km}$ $S = 2.7\,10^{-2}$	${}^{\mathrm{L}}g_{\ell k}^{m}$
I_{st} indexed field	1:3	$< \Delta t$	$R = 2537.\mathrm{km}$ $S = 1.0$	${}^{\mathrm{I}st}g_{\ell k}^{m}$
Induced field	1:6	$< \Delta t$	–	${}^{\mathrm{I}}g_{\ell k}^{m}$
Induced field variation	1:6	$< \Delta t$	–	${}^{\mathrm{I}}\dot{g}_{\ell k}^{m}$
GSM ext. field	1:3	$< \Delta t$	$R = 16000.\mathrm{km}$ $S = 5.4\,10^{3}$	${}^{\mathrm{G}}q_{\ell k}^{m}$
SM ext. field	1:3	$< \Delta t$	$R = 6900.\mathrm{km}$ $S = 3.56$	${}^{\mathrm{S}}q_{\ell k}^{m}$
E_{st} indexed field	1:3	$< \Delta t$	$R = 16000.\mathrm{km}$ $S = 5.4$	${}^{\mathrm{E}st}q_{\ell k}^{m}$
B_y^{IMF} indexed field	1:3	$< \Delta t$	$R = 6900.\mathrm{km}$ $S = 0.1$	${}^{\mathrm{I}}q_{\ell k}^{m}$
Obs. offsets	Non SH	10^6 yr	$R = 6371.2\mathrm{km}$ $S = 1.0\,10^{3}$	$\mathbf{O}_i = (O_x^i, O_y^i, O_z^i)$

Table 2. Summary of all modelled sources, along with the minimum and maximum SH degrees for which they are estimated, the time scale used for the prediction step and information on the way prior spatial covariance matrices were built. The radius R and scaling S are the parameters entering in the definition of the prior as described by Holschneider et al. (2016).

contributions were treated as random errors. As discussed below, in this sequential framework the explicit modelling of the diffusion and truncation errors is necessary to control the temporal variability of the core surface flow.

4 MODELLING METHOD

The set of parameters for the magnetic field contributions and the core surface flow are estimated sequentially in 93 steps, each step spanning three months of data (more precisely 365.25×0.25 days). This is done through a linear Kalman filter (Kalman 1960) in the same way as in Ropp et al. (2020). We provide here only a limited amount of information and refer to Ropp et al. (2020) for details on the process. A Kalman filter can be decomposed in three steps described below: analyse, prediction and smoothing steps. The prediction and analyse steps are made successively for each time interval starting from 1999 up to 2022. When the full series of models and associated covariance matrices is defined, the smoothing steps are applied backward in time.

To start this process – i.e. for the time interval $[t_0, t_1[$, the model parameter prior statistics are required. We assume that all model parameters follow a Gaussian distribution characterised by a mean and a covariance matrix. For the core field parameters, the secular variation, the flow at the top of the core, the diffusion and the truncation errors, the mean model is null, and the covariance matrices are derived from a large number of outputs of the CE numerical dynamo runs. For the truncation errors the covariance matrix also includes a component due to the expected accuracy output of the core field model. For the diffusion, the off-diagonal elements were set to zero. In this way no prior information was provided on the spatial distribution of diffusion. For other sources: lithosphere, magnetosphere, induced sources, the mean models are also null and the covariance matrices are set as in Holschneider et al. (2016) by defining a scaling S and a reference radius R (see table 2). The correlation matrices for the coefficients ${}^{\mathrm{I}}g_{\ell 0}^{m}$ and ${}^{\mathrm{I}}\dot{g}_{\ell 0}^{m}$ have been established by trial and errors as in Ropp et al. (2020). No prior cross-correlations were assumed between independent sources, with the exception of the core and the secular variation, in an attempt to have the best possible resolution of the secular variation for each 3 month interval.

Over a given time interval $[t_k, t_{k+1}[$ the analyse step solves the system of equations (3.7) and therefore updates the means and covariance matrices of equation (3.1) and (3.4) parameters, such that the equations (3.1) fit the observed values of the magnetic field. This is achieved

through an iterative re-weighted least-squares algorithm that at each iteration adjust the Huber weights used for magnetic data, and update the matrix $\mathbf{H}_{^{\mathrm{C}}\mathbf{g}^{\mathbf{m}}_{\ell\mathbf{k}}}$ using the most recent estimates of the Gauss coefficients ${}^{\mathrm{C}}g^m_{\ell k}$. Huber weights are not used for the induction equations (3.4). The covariance matrix of the vector of errors $\mathbf{e_b}$ in equation (3.5) is assumed to be diagonal, and the data variances as a function of the data type are given in table 1. The covariance matrix for the vector of errors $\mathbf{e_f}$ in equation (3.6) is also assumed to be diagonal, and its elements are arbitrarily set to $(\sigma^p)^2 = 10(nT/y)^2$, as a limit for which the equations (3.4) hold. It should be noted that this analyse step separates reasonably well the signals of internal and external origins. However, cross-correlations are generated between parameters of internal origins and between parameters contributing to the induction equations (3.4). These cross-correlations are partially limited by the prior means and covariance matrices of the parameters, but depend mainly on the parameters temporal variabilities that are controlled via the prediction step.

The prediction step carries the information acquired over the time interval $[t_{k-1}, t_k[$ to the next time step $[t_k, t_{k+1}[$. It defines therefore the time dependence of the parameters. As in Ropp et al. (2020), the prediction step of the core field ${}^{\mathrm{C}}g^m_{\ell k}$ parameters is controlled by the estimated secular variation. For all the other parameters their temporal evolutions are described by an order 1 stochastic process depending on one parameter which we refer to as the *time-scale*. The set time-scale values for each parameter type is given in table 2. Note that there is no transfer of information from one time step to the next if the time-scale is shorter than the time step. The temporal dependencies play a major role in the separation of the "induced" contributions (parameters ${}^{\mathrm{I}}g^m_{\ell k}$ and ${}^{\mathrm{I}}\dot{g}^m_{\ell k}$) from the core field contributions, or, as this will be discussed below, in the separation of the diffusion and truncation errors from the advection term in the induction equation.

The last step of the Kalman filter is the smoothing. It carries backward in time the information derived at recent epochs. The process applied is exactly the same as in Ropp et al. (2020). It smoothes the parameter time series and, in particular, shifts slightly backward in time the estimated secular variation.

5 RESULTS

The results are presented in this section in three parts: we start with the presentation of the fit to the data, then look at the general features of the core field model, and finish

with a description and analysis of the flow model. We recall that the outputs of the modelling process are Gaussian distributions of models characterised by their mean values and covariance matrices. In the following, unless specified, the term "model" refers to the mean model. The combination of core field and secular variation models we derived is called the MCM-2022 model.

5.1 Fit to the data

The evolution in time of the standard deviations (STDs) of the estimated error terms $\mathbf{e}_o$ and e_f in equations (3.1) and (3.4) gives a good idea of the quality of the model fit to the data. These STDs are estimated over each time step, before the Kalman smoothing process. In Figure (2) are presented these STDs for the weighted error terms, where the weight for the magnetic datum i is:

$$w_i = \frac{\sqrt{w_{hi}}}{\sigma_i^p} \tag{5.1}$$

where w_{hi} is the Huber weight (for most of the data $w_{hi} = 1$), and σ_i^p the prior STD associated with the data (see Table 1). For the flow equations, Huber weights were not used and the weights are simply $w_i = 1/\sigma_i^p$.

In Figure (2) left, it seems that the prior STDs of the high latitude data may be under-estimated leading to high values of the weighted residual STDs, but the residual distributions are not Gaussian. They present large tails (larger even than those expected for a Laplacian distribution) and therefore the STD is not a good estimate of the fit to the data. What is important is that all the STDs are relatively constant over time. For low latitude data the fit is as good as expected with posterior STDs around 1. Otherwise, a variability of the fit linked to the Solar cycle can be seen. For the flow equations, the residual STDs (Figure 2, right) are very small; the prior variances for e_f were probably too large. This has apparently no effect on the quality of the results. We observe nonetheless a regular decrease of the posterior STDs over the first four years, possibly linked with the robustness of the secular variation that increases over the years as more data are assimilated (Fournier et al. 2021).

5.2 Magnetic field model

The core field and secular variation Gauss coefficients can be extracted from the series of snapshot models fitted to the data. Along the ∼22 years time-span of the model, both the core field and its secular variation vary in time. They present however identified structures at

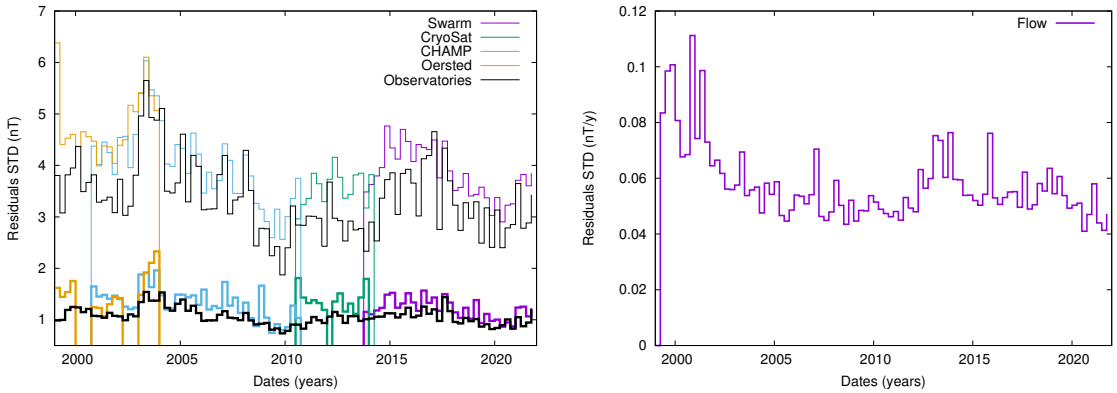

Figure 2. Standard deviations of the weighted residuals from (left) the model fit to the magnetic data (values are estimated without separating vector components, thick lines are used for mid and low latitude data, thin lines for high-latitude data) and (right) the flow model fit to the secular variation.

the core mantle boundary (i.e. at radius c=3485 km) that are shown for year 2015, well inside the Swarm era, in Figure (3). The core field presents the usual sinuous magnetic equator, and patches in the southern hemisphere where the radial component of the core field has a sign opposed to the expected positive value associated with a pure dipole field. The secular variation is dominated by small scale patterns, with large values under North-East Siberia, not far from the imprint of the inner core tangent cylinder on the core mantle boundary, and patches of strong radial values at low latitudes in between $[-90 : +120]$ degrees in longitudes (positive eastward).

The time series of the core field and secular variation Gauss coefficients allow the secular variation and acceleration to be estimated using a three point finite difference formula (see

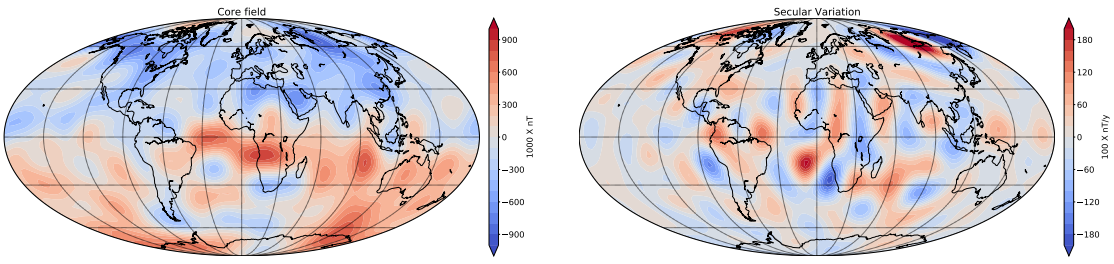

Figure 3. Snapshots of the core and secular variation magnetic field model radial components, truncated to spherical harmonic degree 13, for year 2015.0 and estimated at the core mantle boundary. Continents are shown to help understanding the field geometry.

Abramowitz & Stegun 1964, eq. 25.3.4). In Figure (4) are presented the temporal evolution of the secular variation Gauss coefficients ${}^{\mathrm{C}}\dot{g}_1^0$, ${}^{\mathrm{C}}\dot{g}_3^{-3}$, ${}^{\mathrm{C}}\dot{g}_5^0$ and ${}^{\mathrm{C}}\dot{g}_8^8$ as estimated through the modelling process and compared to the CHAOS-7 model (Finlay et al. 2020). As in Ropp et al. (2020), the agreement with CHAOS is not very good for the ${}^{\mathrm{C}}\dot{g}_1^0$ coefficient but is better for other coefficients. Our MCM-2022 model generally presents a higher temporal resolution. We also observe the consistency of the secular variation as estimated from the data with the secular variation calculated by finite differences from the estimated ${}^{\mathrm{C}}g_{\ell k}^m$ time series. This is an important point to verify when co-estimating the magnetic field and the flow models.

The energy as a function of the wavelengths for the core field, the secular variation and acceleration are shown in Figure (5, left), for three different epochs. When compared to the priors derived from the (CE) dynamo model, these spectra show that there is more energy than expected in the core field and secular variation above spherical harmonic degree 14, possibly due to un-modelled or poorly modelled sources at these wavelengths. On the same figure are presented the temporal evolution of the secular variation and acceleration energies over time, truncated to spherical harmonic 13. There is a very significant increase of the secular variation energy around 2009, that reaches a maximum in 2019. The same behaviour is observed for the CHAOS-7.9 model (Finlay et al. 2020) and is mainly due to an increase of the secular variation energy at large scales (spherical harmonic degrees smaller than 5). There is a clear $\sim$3 years periodicity in the secular acceleration energy, suggesting a dominant periodicity around 6 years in the secular variation and acceleration signals. Therefore, unsurprisingly, the time scale for the acceleration defined by:

$$\tau_{\mathrm{SA}}(\ell, k) = \sqrt{\frac{\sum_m ({}^{\mathrm{C}}\dot{g}_{\ell k}^m)^2}{\sum_m ({}^{\mathrm{C}}\ddot{g}_{\ell k}^m)^2}} \tag{5.2}$$

where ${}^{\mathrm{C}}\ddot{g}_{\ell k}^m$ are the Gauss coefficients of the acceleration centred on the time interval $[t_k, t_{k+1}[$, gives values around 6 or 7 years for spherical harmonic degrees between 5 and 13, as in Ropp et al. (2020) (see Figure 6). This result gives us confidence in the quality of the modelled secular variation and acceleration up to degree 13. For higher degrees the estimated acceleration time scales are not accurate, as the secular variation energy is too large.

5.3 Core surface flow model

As for the core field, the toroidal and poloidal flow coefficients can be extracted from the series of snapshot models fitted to the data. This gives a series of 93 snapshot flow models, $\sim$3 months apart. They all present the general patterns described in Pais & Jault (2008) charac-

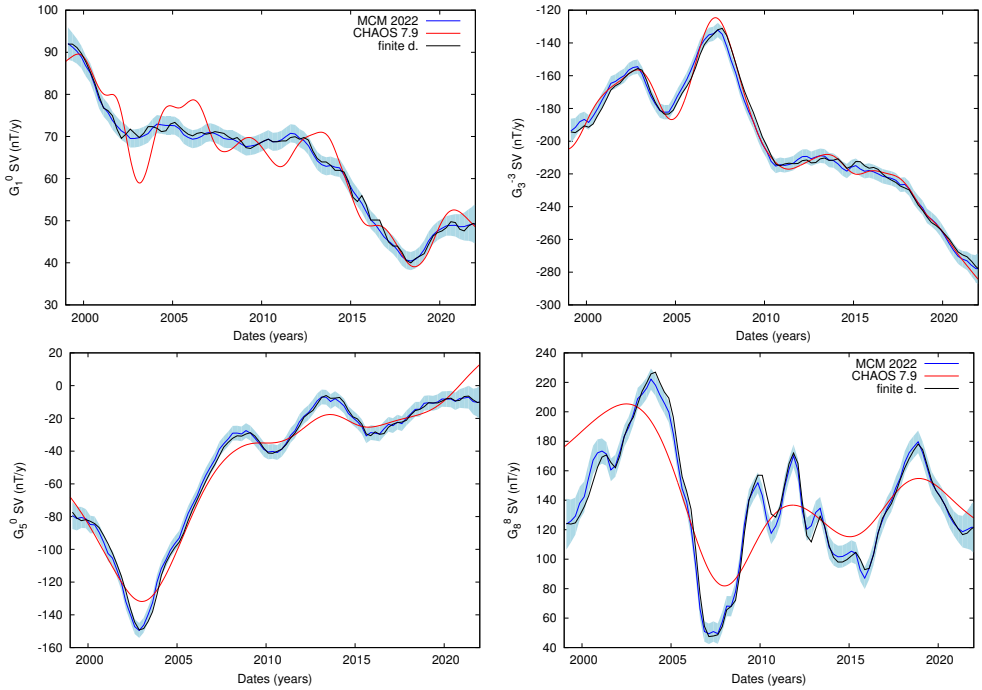

Figure 4. Temporal evolution of the secular variation of the ${}^{\mathrm{c}}\dot{g}_1^0$, ${}^{\mathrm{c}}\dot{g}_3^{-3}$, ${}^{\mathrm{c}}\dot{g}_5^0$ and ${}^{\mathrm{c}}\dot{g}_8^8$ coefficients. Outputs of the MCM 2022 model are in blue with their 2-sigma error interval indicated. In black are shown the values estimated by finite differences from the time series of core field coefficients ${}^{\mathrm{c}}g_{\ell k}^m$, and in red the outputs from the CHAOS-7.9 model.

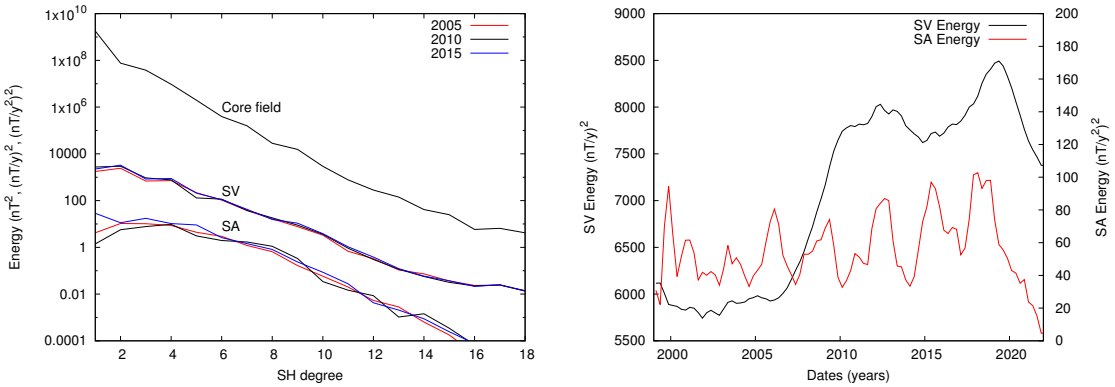

Figure 5. Left: Energy spectra as a function of the wavelength for the core magnetic field, its secular variation and acceleration at three different epochs. Right: Evolution in time of the secular variation and acceleration energies (models have been truncated at spherical harmonic degree 13). All quantities are estimated at the Earth's surface. The acceleration is estimated by a three-points finite difference scheme applied on the secular variation model. Its energy estimates before 2001 and after 2020 are not as robust as in between 2001 and 2020.

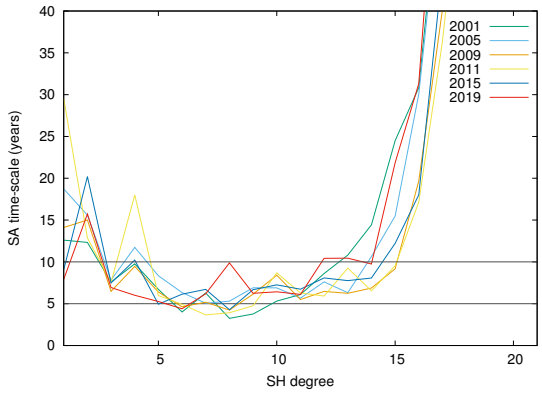

Figure 6. Acceleration time-scale for a selection of dates, as derived from the secular variation model.

terised by a large scale gyre, essentially invariant along the rotation axis of the Earth, flowing westward close to the inner-core tangent cylinder in the Pacific hemisphere, but flowing along the core mantle boundary in the African hemisphere (see Figures 7, top row). The energy of this flow as a function of spherical harmonic degree is shown in Figure (8, left) for three different epochs, independently for the toroidal and poloidal components, and together with their prior and posterior statistics. It is obvious than only a small part of the flow coefficients are robustly estimated. To extract the robust part of the flow we used the posterior covariance matrix of the flow (see Appendix B), and present "resolved" flow estimates in Figures (7) (bottom row). Although small-scale flow patterns are visible, the resolved flow still presents the large scale gyre identified in Pais & Jault (2008). The main evolution of the flow patterns in between 2006 and 2019, is concentrated under the western part of the Pacific Ocean. There is also a strengthening of the flow at high latitudes. To this variability of the flow corresponds an evolution of the flow energy over time which is presented in Figure (8, right). Although the flow energy increases over time there is no obvious correlation with temporal evolution of the secular variation energy. This may be due to the excess of flow energy associated with the geomagnetic Jerk for year 2006 (Chulliat et al. 2010). The clear 3-year periodicities of the core field acceleration energy are not matched by similar variations in the flow acceleration energy (not shown).

With only a $\sim$22 year time-span and 93 snapshots the flow model is too short to study its variability through a detailed Fourier analysis. To better describe how the flow is evolving over the model time-span, we made a principal component analysis of the model snapshots – see Appendix C. The first three modes are presented in Figure (9) together with their time variations. The first mode presents the usual large scale gyre, flowing westward at a speed

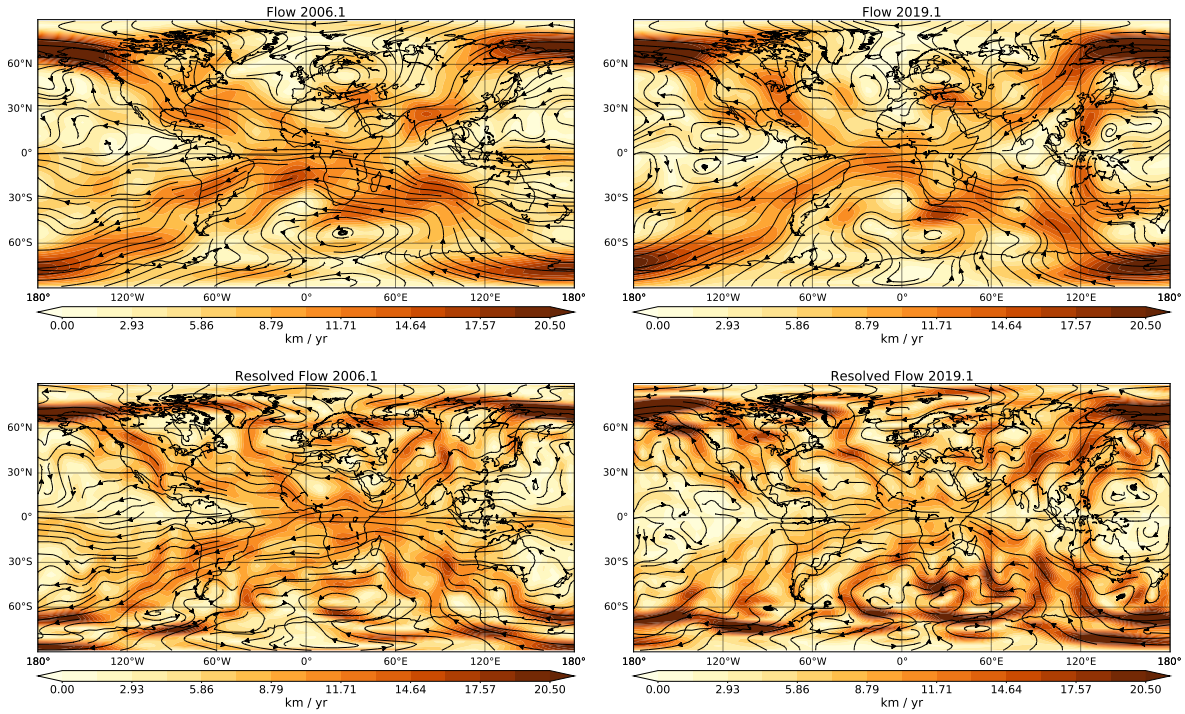

Figure 7. Core surface flow for year 2006 (left) and 2019 (right). Top row: the flow model is truncated to spherical harmonic degree 13. Bottom row: the "resolved" part of the flow (see Appendix B) up to spherical harmonic degree 26 is shown. Arrows indicate the flow directions and the colormap the flow speed. The flow map presents a strong north-south symmetry compatible with quasi-geostrophic flows. Continents are shown to help understanding the flow structure.

of few km/y at the equator, in the African hemisphere. It is essentially constant over time, although a variability of the order of 1 km/y is observed (with also some periodicity) for its scaling factor. The main variability of the flow is carried by the modes 2 & 3 that are strongly symmetric relative to the equator. These modes are characterised by small gyres flowing eastward at the equator and westward at higher latitudes. High-latitude flows are mainly westward for the mode 2, and eastward for the mode 3. However these flow directions change with time. The mode-2, with gyres centred at longitude 160^o East, has a multiplicative factor varying by 4 km/y over the model time-span. These gyres therefore flow first westward at the equator, vanish around 2012.7, and flow eastward after this date. Similarly the mode-3 has gyres centred at longitude 80^o East. They flow at the equator first East, then West, and finally back to East. Very similar results are obtained for the first three modes when analysing the "resolved" flow. It should be noted that the decomposition of the first three modes into a first mode nearly constant in time, a second mode presenting a linear trend and a third mode with a quadratic behaviour in time, comes naturally in a principal component analysis and

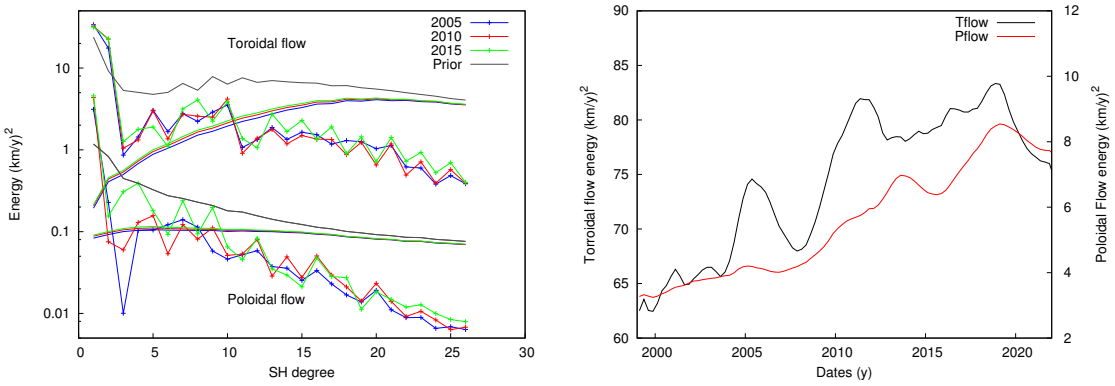

Figure 8. Left: Energy spectra as a function of the wavelength for the toroidal (top line-point curves) and poloidal (bottom line-point curves) flows. Prior energies are indicated with black continuous lines. Posterior energies of the flow model errors are indicated with coloured continuous lines. Right: Evolution in time of the toroidal and poloidal flow energies. The energy of the poloidal flow is one order of magnitude smaller than the toroidal energy. Energy estimates before 2001 and after 2020 are not as robust as between 2001 and 2020.

is not necessarily linked to the dynamics of the flow. The approach clearly shows that the main flow variations at mid- or low-latitudes are in between longitude interval $[60^o, 210^o]$ East, however it is not well suited to extract signatures of torsional oscillations or MC eigenmode flows.

With the aim of identifying torsional waves, we focus now on the flow azimuthal component. In Figure (10) top row, left, is presented the east component of the modelled flow at the magnetic equator as a function of time. This component presents a generally strong westward flow with, in 2000, two areas of lower velocities at longitude 100^o East and around 260^o East. These area are still present in 2012, but seem to merge forming a larger patch of low flow velocity that even switches to eastward flow in 2019. Still in Figure (10) top row, left, can be distinguished a light periodicity with time. In order to better highlight this periodicity, the flow model has been filtered by fitting and then removing sine and cosine waves with frequencies $\nu_k = k\,\delta\nu$ ($k = 0, 1, 2$ and $\delta\nu = \frac{1}{23.25}\,y^{-1}$) to the time series of flow spherical harmonic coefficients. In Figure (10) top row, right, is presented the east component of the filtered flow model at the magnetic equator as a function of time. It exhibits patterns, particularly strong after 2013, with fast westward propagation (e.g. from $\sim 249^o$ to $\sim 159^o$ longitude over 1.5 years, i.e. roughly $\sim 60^o$ longitude per year) and strong periodicities of $\sim$7 years, very similar to the patterns described by Gillet et al. (2022). They have been identified by these authors as the signatures of MC eigenmodes (Gerick et al. 2021). However the comparison does not

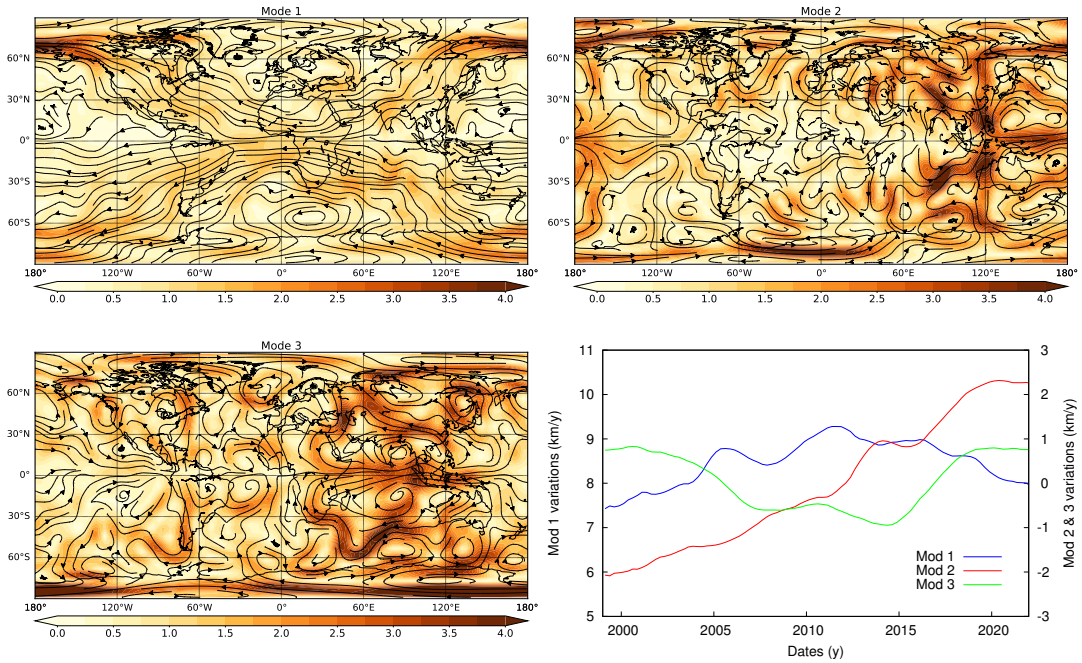

Figure 9. Three first principal components of the core surface flow model together with their temporal evolutions. The flow patterns have no units, but are all presented with the same scale. The maximum spherical harmonic degree is 26. Their temporal evolutions are multiplicative factors that have units of km/y. Continents are shown to help understanding the flow structure.

hold when comparing the propagation speed (estimated to $\sim 25^o$ longitude per year by Gillet et al. (2022)) and when displaying the latitudinal eastern filtered flow structure as a function of time for longitude 170^o East (see Figure 10, bottom row, left): there are strong azimuthal flows centred at colatitudes 60^o and 120^o, in opposite direction compared to those at the equator. There are also significant contributions at higher latitudes, with weak evidences of a pole-ward drift with time. At high latitudes, signals have shorter periods that we did not smooth out in our approach (in Gillet et al. (2022), periods shorter than 4 years are filtered out). To have a better view of the spatial patterns of the filtered flow, a map of its eastward component is displayed in Figure (10) bottom row, right, for epoch 2017.6. It presents patches of alternate eastward and westward flow on the equator, with a maximum flow in the Pacific hemisphere and a vanishingly small flow under the Atlantic. To these patches correspond further patches at higher latitudes, symmetrical relative to the equator, with azimuthal flows in opposite directions.

The general picture provided by the filtered flow is therefore the presence of small columnar flows along the equator, with their rotation axis aligned with the Earth's rotation axis and

roughly centred between 10^o and 15^o latitude. These columnar flows are perturbations around a slowly varying flow. They have higher velocities at longitudes $\sim 250^o$ East and $\sim 150^o$ East. From the successive snapshot models of the filtered flow, it is difficult to established if these columnar flows are drifting in longitudes or are independent structures fed by higher latitude perturbations. They have however an apparent westward propagation speed of $\sim 60^o$ longitude per year. They are strongly reduced at longitude $\sim 100^o$ East, very likely because of the geometry of the large scale gyre described by Pais & Jault (2008). Although weaker, they can still be identified in the African hemisphere. The flow speed in these columnar flows seems to be not exceeding $\sim 5 km/y$ in the Pacific hemisphere where they are the main observed flow variations. This system of columnar flows propagating westward is consistent with the general flow evolution highlighted in Figure (9) and is very likely the source of the observed core magnetic field acceleration in the Pacific hemisphere.

We note that between 2005 and 2015, the same westward propagating patterns are observed under the Atlantic (see Figure (10) top row, right, between longitudes 300^o and 350^o East). As in the Pacific hemisphere, the corresponding core flow is made up of small columnar flows propagating west. They are probably associated with the core magnetic field acceleration observed over the same period in the African hemisphere.

6 DISCUSSION

In the previous section results of our modelling work have been presented with a focus on the core magnetic field and core surface flow models together with their temporal variations at mid- and equatorial latitudes. These variations are a consequence of modelling choices that we discuss here.

The variability of the core surface flow model follows from the variability of the magnetic field model. The latter presents the expected characteristics with in particular a secular acceleration energy having 3-year periodicities (see Figure 5). This suggest that 6-year periodicities are present in the secular variation and acceleration models. However these periodicities are harmonics of the solar cycle, and the associated activity of magnetic external fields may have leaked e.g. through the induced field signals or poorly modelled high latitudes ionospheric signals, inside the core field and secular variation models (e.g. see Lesur et al. (2022); Finlay et al. (2017)). To limit as much as possible these leakages we introduced an induced field model parameterised by the ${}^{\mathrm{I}}g_{\ell k}^m$ and ${}^{\mathrm{I}}\dot{g}_{\ell k}^m$ Gauss coefficients (see Table 2 and Equation 3.1).

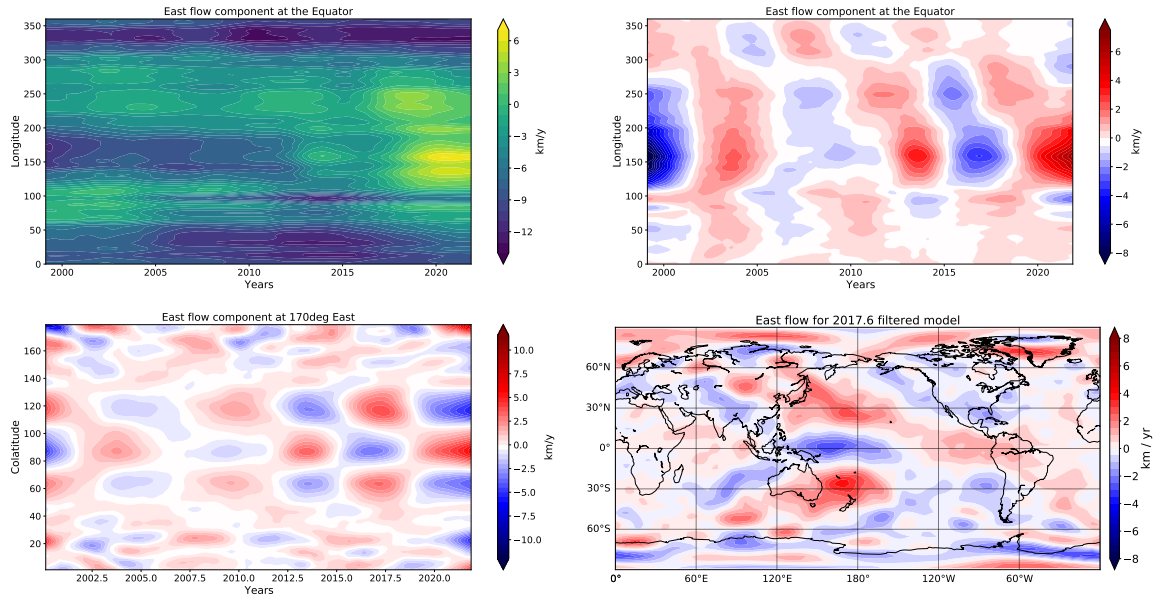

Figure 10. First row: Longitude-time plots of the eastward core surface flow estimated at the equator. The full flow model is shown on the left, the filtered version on the right. Second row: latitude-time plot of the eastward component of the filtered core surface flow at longitude 170^o East is shown on the left, the map of the eastward filtered flow component at epoch 2017.6 is on the right. It is centred on the Pacific Ocean. Continents are shown to help understanding the flow structure.

The prior time-scale for these parameters is very short (smaller than the Kalman stepping interval), and therefore they characterise well fast field variations. Their amplitudes have been tuned so that they describe the annual periodicities that appears naturally in internal magnetic field models fitted to observatory and satellite magnetic data. On the other hand these amplitudes are sufficiently small so as not to affect significantly the 6-year periodicities observed in the magnetic field secular acceleration. It is clear however that these priors are set rather arbitrarily: we are not able to asses if part of the annual variability of the induced field is due to core processes, or if the 6-year periodicities in the secular variation are partly due to external sources activity. However, the secular acceleration patterns are observed mainly at mid- or low-latitudes and there is a general agreement that they are of core origin (e.g. Olsen & Mandea (2008); Lesur et al. (2008); Chulliat et al. (2010)).

Identifying time varying patterns in the flow model heavily depends on the way the induction equation (equations 3.3, 3.4) is parameterised. In our approach, there are three modelled "sources" that can account for the observed secular variations: the core surface flow, the diffusion and the truncation errors. They are treated here has independent "sources", with no prior cross-correlation between them and their contributions to the secular variation cannot

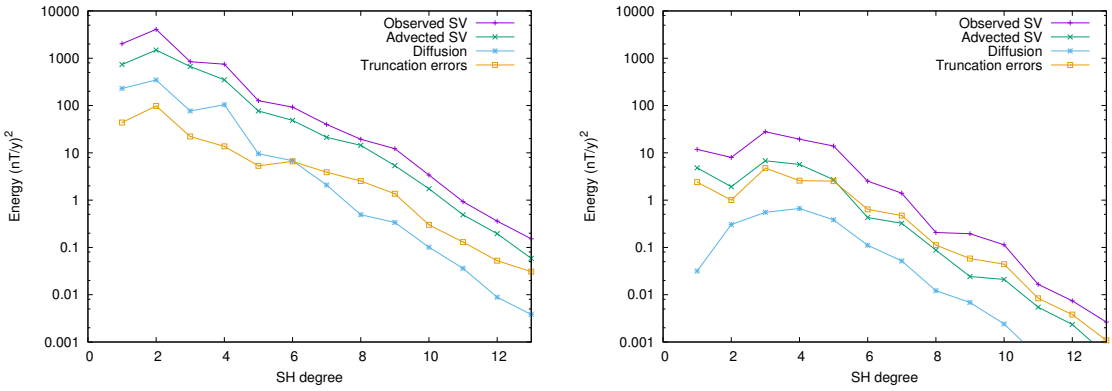

Figure 11. Left: Energy at the Earth's surface and for epoch 2017.62, as a function of the spherical harmonic degree for the observed secular variation, its component resulting from the advection of the core field by the flow, the diffusion and the truncation errors. Right: The same derived from filtered quantities. Note that the filtered advected secular variation energy is the energy of the secular variation component resulting from the advection of the core field by the filtered flow and not the filtered version of the advected secular variation. These are different quantities as the core field varies with time.

be separated from equation (3.4) alone. It is only through their prior time-scales and amplitudes that this separation is possible (see Table 2). The secular variation generated by the time averaged core flow does not separate well from the time average diffusion and truncation errors. However, the former contribution prior and posterior amplitudes are much larger than the amplitudes of the two latter contributions (see Figure 11, left), thus the averaged surface core flow is reasonably accurate. We consider now only temporal variations of the core surface flow. Figure (11), right, shows the energy as a function of wavelength for different filtered contributions. The weakness of the filtered diffusion spectrum, compared to the spectrum displayed on the left plot, is a clear indication that diffusion varies only slowly with time and therefore separate well from the advection contribution for periods shorter than $\sim$11 years. This smooth variation of diffusion contribution in time is in agreement with its prior time-scale that was set to that of the core field model (see Table 2). The time-scale of the truncation errors has been set to that of the secular variation model: it is not much smaller than the time-scale of the core flow (see Table 2). It follows that the truncation error contribution is the least affected by the filtering process. Therefore, truncation errors describe a significant part of the secular variation rapid evolution, but not the slowest variations.

Despite these difficulties in the separation of the core flow, the diffusion and the truncation errors, there are flow variation patterns that are reliable. These are described by the first

three modes in Figure (7). These core flow variations generate a secular variation that is too large to be explained by small amplitude truncation errors or diffusion signals. Even if the time-scale of these two latter "sources" are dropped to values smaller than the Kalman filter time step, the modelled core flow still present the same large amplitude slow variation patterns.

We expected that the 6-year periodicities of the secular variation translate in some characteristic patterns with the same periodicities in the core surface flow. We identified the signature of westward propagating columnar flows (see Figure 10) with a period close to 7 years. This 7-year periodicity should be interpreted with caution as the third harmonic $\nu_3 = 3\,\delta\nu$ ($\delta\nu = \frac{1}{23.25}\,y^{-1}$) of the filtering process we applied, leads to a periodicity of 7.75 years. This periodicity is thus likely to emerge naturally in the filtered quantities. A closer analysis of the filtered flows shows that they are also affected by edge effects before 2001 and after 2020. However, at no point in the process did we favour westward propagation of the observed patterns (see Figure 10 top, right) that clearly results from the inversion of the data. Neither the longitudinal propagation speed (60^o per year), nor the latitudinal structure of the signals we obtained match those of the signals, otherwise very similar, described by Gillet et al. (2022) and identified by these authors as MC eigenmodes (Gerick et al. 2021). The spread to mid-latitudes of the periodic patterns we observe (see Figure 10 bottom, left) could be due to the Couple-Earth (CE) dynamo model (Aubert et al. 2013) that we used to build our prior. Using the model described in Aubert (2019) that separates advection from waves in the core flow, may help concentrating the kinetic energy near the equator and lead to results closer to those obtained by Gillet et al. (2022). Yet we note that the same filtering process applied to the "resolved" flow, that is less dependent on the prior, leads to the same patterns with generally smaller scale structures (see Figure 12). It is however difficult to be confident that the signals we observed are, or are not, MC eigenmodes, since the signatures of the latter at the core surface depend on the magnetic field inside the core that is probably more complex than the simple model used by Gerick et al. (2021). There are also other propagating waves in the core – e.g. QG-Alfen waves (Aubert 2019; Aubert & Gillet 2021) or, in case of stratification, MAC waves (Buffett & Matsui 2019), although in both cases the theoretical flows are not, at first glance, comparable to our observed flow patterns.

We have not explored in detail what would be the effect of adding prior cross-correlations between core flow, diffusion and truncation errors, nor adding prior cross-correlations between them and the secular variation. This may slightly improve the posterior cross-correlation, but

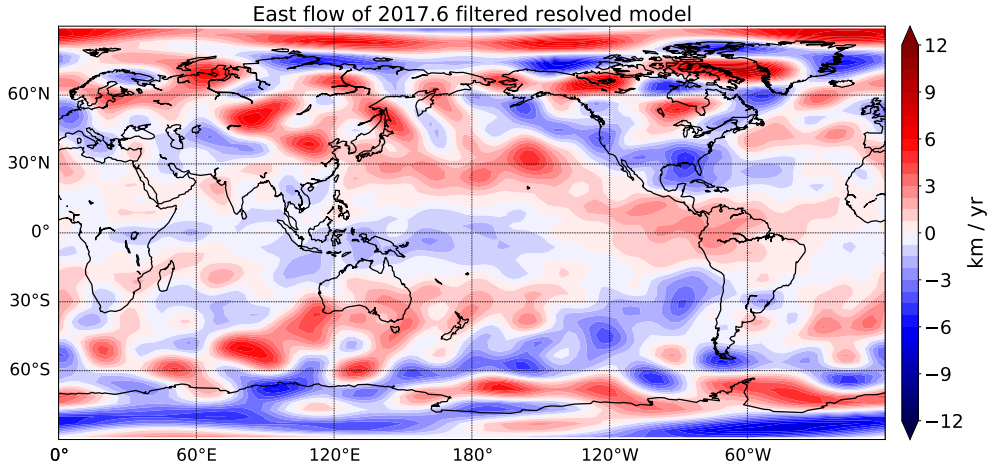

Figure 12. Map of the eastward core surface flow at epoch 2017.6 derived from the filtered resolved part of the model (threshold ratio=2, see appendix B). Continents are shown to help understanding the flow structure.

as these are not resolved by the data it is likely that the posterior cross-correlations remain those of the prior cross-correlations.

As a final remark, we point out that we have not been able to identify torsional waves as in Gillet et al. (2010) probably because our time-series of core surface flow models is two short to get good frequency resolution and separate a 5-year period from other periods. However, that does not rule out the presence of these waves in our model or in the data.

7 CONCLUSION

The Earth's magnetic field and associated core surface flow have been modelled from 1999 to 2022, from satellite magnetic data and ground observatory hourly means. The technique used relies on a Kalman filter and a covariance based modelling approach (Holschneider et al. 2016; Ropp et al. 2020). The output of this modelling process is a series of snapshot gaussian distributions defined by a mean model and a covariance matrix. The core magnetic field model has the same characteristics as the model described in Ropp et al. (2020). It compares well with the other core field models (– e.g. Finlay et al. 2020), but generally shows a larger variability in time. The co-estimated core surface flow model presents a quasi-geostrophic large-scale gyre already identified by Pais & Jault (2008).

In order to study the variability of the core flow, it has been necessary to co-estimate the diffusion and truncation-error parts of the induction equation such that their temporal variability could be controlled. We found that the temporal variations of the core flow and truncation errors are particularly difficult to separate. Nonetheless we identified an increasing flow speed at high latitudes, and significant flow variations under the western part of the Pacific Ocean. We also identified periodic azimuthal flows propagating westward over $\sim 60^o$ longitude per year. These periodic signals are associated with columnar flow structures along the equator under the Pacific Ocean. The same flow structure has been observed under the Atlantic Ocean, from 2005 to 2015. Although they have a periodicity around $\sim$7 years, they cannot be immediately identified as Magneto-Corriolis (MC) eigenmodes (Gerick et al. 2021; Gillet et al. 2022) because they present larger scale structures in the latitudinal direction. However, none of our results rule out the presence of these MC eigenmodes or torsional waves with shorter time periodicities

In order to verify the robustness of our results, we use the output core surface flow model covariance matrix to extract the part of the surface flow that is the best resolved. This "resolved" flow present the same characteristics as the full flow model, giving us confidence in our results. However, the presence and characteristics of the identified columnar flows have to be confirmed and further studied. They are still open questions such as the apparent weakness of these flow structures under Africa, or their abrupt weakening at longitude 100^o East as they propagate westward. It is essential to pursue the magnetic data acquisition on ground and through satellite missions to better understand and describe the flow variation patterns that we have started to properly identify thanks to the high quality magnetic data accumulated over the last two decades.

ACKNOWLEDGMENTS

We thank Thomas Gastine and Alexandre Fournier for their supports and encouragements. This work was partly supported by the CNES grants "Suivi et exploitation de la mission Swarm" and "Kourou observatory" projects and by ESA (contract 4000109587/13/I-NB Swarm ESL/SW-CO-DTU-GS-010). This modelling work would not be possible without the contributions from observers in ground magnetic observatories and the work of the INTERMAGNET organisation. We thank two anonymous reviewers for their thorough reviews that help improving the manuscript.

Availability of data and materials

The data used in this study are all available on international databases. In particular:

- Data from Oersted satellite are available at:

`ftp://ftp.spacecenter.dk/data/magnetic-satellites/Oersted`

- Data from CHAMP satellite are available at:

`https://isdc.gfz-potsdam.de/champ-isdc/access-to-the-champ-data/`

- Data from CryoSat-2 satellite are available at:

`https://swarm-diss.eo.esa.int/#swarm%2FMultimission`

- Data from Swarm satellites are available at:

`https://swarm-diss.eo.esa.int/#swarm%2FLevel1b`

- Magnetic observatory data are available at:

`ftp://ftp.nerc-murchison.ac.uk/geomag/Swarm/AUX_OBS/hour/`

REFERENCES

Abramowitz, M. & Stegun, I. A., 1964. *Handbook of mathematical functions*, Dover Press, New York.

Asari, S. & Lesur, V., 2011. Radial vorticity constraint in core flow modeling, *Journal of Geophysical Research - Solid Earth.*, **116**(B11101), doi: 10.1029/2011JB008267.

Aubert, J., 2019. Approaching earths core conditions in high resolution geodynamo simulations, *Geophysical Journal International*, **219 S1**, S137–S151, doi: 10.1093/gji/ggz232.

Aubert, J. & Gillet, N., 2021. The interplay of fast waves and slow convection in geodynamo simulations nearing Earths core conditions, *Geophysical Journal International*, **225**(3), 1854–1873, doi: 10.1093/gji/ggab054.

Aubert, J., Finlay, C. C., & Fournier, A., 2013. Bottom-up control of geomagnetic secular variation by the Earth's inner core, *Nature*, **502**, 219–223, doi: 10.1038/nature12574.

Baerenzung, J., Holschneider, M., & Lesur, V., 2014. Bayesian inversion of the filtered flow at the earth's core mantle boundary, *J. Geophys. Res. Solid Earth*, **119**, doi: 10.1002/2013JB010358.

Baerenzung, J., Holschneider, M., & Lesur, V., 2016. The flow at the Earth's core mantle boundary under weak prior constraints, *Journal of Geophysical Research (Solid Earth)*, **121**(3), 1343–1364, doi: 10.1002/2015JB012464.

Baerenzung, J., Holschneider, M., Wicht, J., Sanchez, S., & Lesur, V., 2018. Modeling and predicting the short term evolution of the geomagnetic field, *Journal of Geophysical Research: Solid Earth*, **123**, doi: 10.1029/2017JB015115.

Barrois, O., Gillet, N., & Aubert, J., 2017. Contributions to the geomagnetic secular variation from a reanalysis of core surface dynamics, *Geophysical Journal International*, **211**(1), 50–68, doi: 10.1093/gji/ggx280.

Barrois, O., Hammer, M., Finlay, C., Martin, Y., & Gillet, N., 2018. Assimilation of ground and satellite magnetic measurements: inference of core surface magnetic and velocity field changes,, *Geophys. J. Int.*, **215**(1), 695–712, doi: 10.1093/gji/ggy297.

Beggan, C. D. & Whaler, K. A., 2009. Forecasting change of the magnetic field using core surface flows and ensemble kalman filtering, *Geophys. Res. Lett.*, **36**(18), doi: 10.1029/2009GL039927.

Bloxham, J., 1988. The determination of fluid flow at the core surface from geomagnetic observations, in Mathematical Geophysics, A Survey of Recent Developments in Seismology and Geodynamics, pp. 189–208, eds Vlaar, N. J., Nolet, G., Wortel, M. J. R., & Cloetingh, S. A. P. L., Reidel, Dordrecht.

Bloxham, J., 1990. On the consequences of strong stable stratification at the top of the Earth's outer core, *Geophys. Res. Lett.*, **17**, 2081–2084, 10.1029/GL017i012p02081.

Buffett, B. & Matsui, H., 2019. Equatorially trapped waves in Earths core, *Geophysical Journal International*, **218**(2), 1210–1225, doi: 10.1093/gji/ggz233.

Chulliat, A., Thébault, E., & Hulot, G., 2010. Core field acceleration pulse as a common cause of the 2003 and 2007 geomagnetic jerks, *Geophys. Res. Lett.*, **37**(L07301), doi: 10.1029/2009GL042019.

Courtillot, V. & Le Mouël, J.-L., 1988. Time variations of the Earth's magnetic field: from daily to secular, *Ann. Rev. Earth Planet. Sci*, **16**, 389–476.

Courtillot, V., Ducruix, J., & Le Mouël, J.-L., 1978. Sur une accélération récente de la variation séculaire du champ magnétique terrestre, *C. R. Acad. Sci. Paris. Ser. D*, **287**, 1095–1098.

Eymin, C. & Hulot, G., 2005. On core surface flows inferred from satellite magnetic data, *Phys. Earth Planet. Inter.*, **152**(3), 200–220, doi: 10.1016/j.pepi.2005.06.009.

Finlay, C. C., Lesur, V., Thébault, E., Vervelidou, F., Morschhauser, A., & Shore, R., 2017. Challenges handling magnetospheric and ionospheric signals in internal geomagnetic field modelling, *Space Science Reviews*, **206**, 157–189, doi: 10.1007/s11214-016-0285-9.

Finlay, C. C., Kloss, C., Olsen, N., Hammer, M. D., Tffner-Clausen, L., Grayver, A., & Kuvshinov, A., 2020. The chaos-7 geomagnetic field model and observed changes in the south atlantic anomaly, *Earth, Planets and Space*, **72**(1), 156, doi: 10.1186/s40623-020-01252-9.

Fournier, A., Aubert, J., Lesur, V., & Thbault, E., 2021. Physics-based secular variation candidate models for the IGRF, *Earth, Planets and Space*, **73**(1), 190, doi: 10.1186/s40623-021-01507-z.

Gauss, C. F. & Weber, W., 1839. *Resultate aus den Beobachtungen des Magnetischen Vereins. - 1836(1837) - 1841(1843) nachgewiesen, 1838 (1839)*, Weidmann (Leipzig).

Gerick, F., Jault, D., & Noir, J., 2021. Fast quasi-geostrophic magneto-coriolis modes in the earth's core, *Geophysical Research Letters*, **48**(4), e2020GL090803, doi: 10.1029/2020GL090803.

Gibson, R. & Roberts, P. H., 1969. The Bullard-Gellman dynamo, in Applications of Modern Physics to the Earth and Planetary Interiors, pp. 577–602, ed. Runcorn, S.

Gillet, N., Pais, M., & Jault, D., 2009. Ensemble inversion of time-dependent core flow models., *Geochem. Geophys. Geosyst.*, **10**(Q06004), doi: 10.1029/2008GC002290.

Gillet, N., Jault, D., Canet, E., & Fournier, A., 2010. Fast torsional waves and strong magnetic field

within the Earth's core, *Nature*, **465**, 74–77, doi: 10.1038/nature09010.

Gillet, N., Huder, L., & Aubert, J., 2019. A reduced stochastic model of core surface dynamics based on geodynamo simulations, *Geophysical Journal International*, **219**(1), 522–539, doi: 10.1093/gji/ggz313.

Gillet, N., Gerick, F., Jault, D., Schwaiger, T., Aubert, J., & Istas, M., 2022. Satellite magnetic data reveal interannual waves in Earths core, *PNAS*, doi: 10.1073/pnas.2115258119.

Holme, R., 2007. Large-scale flow in the core, in Treatise on Geophysics, vol. 8, ed. Kono, M., Elsevier Ltd., Amsterdam.

Holme, R., 2015. 8.04 - large-scale flow in the core, in Treatise on Geophysics (Second Edition), pp. 91–113, ed. Schubert, G., Elsevier, Oxford, second edition edn., doi: 10.1016/B978-0-444-53802-4.00138-X.

Holschneider, M., Lesur, V., Mauerberger, S., & Baerenzung, J., 2016. Correlation based modelling and separation of geomagnetic field components, *J. Geophys. Res. Solid Earth*, **121**, 3142–3160, doi: 10.1002/2015JB012629.

Kalman, R., 1960. A new approach to linear filtering and prediction problems., *J. Basic Eng.*, **82**, 35–45, doi: 10.1115/1.3662552.

Le Mouël, J., Gire, C., & Madden, T., 1985. Motions at core surface in the geostrophic approximation, *Physics of the Earth and Planetary Interiors*, **39**(4), 270–287, Special Issue Irregularities in the Secular Variation and Geodynamic Implication, doi: 10.1016/0031-9201(85)90140-2s.

Lesur, V. & Vervelidou, F., 2020. Retrieving lithospheric magnetisation distribution from magnetic field models, *Geophys. J. Int.*, **220**, 981–995, doi: 10.1093/gji/ggz471.

Lesur, V., Macmillan, S., & Thomson, A., 2005. A magnetic field model with daily variation of the magnetopsheric field and its induced counterpart in 2001, *Geophys. J. Int.*, **160**(1), 79–88, doi: 10.1111/j.1365-246X.2004.02479.x.

Lesur, V., Wardinski, I., Rother, M., & Mandea, M., 2008. GRIMM - The GFZ Reference Internal Magnetic Model based on vector satellite and observatory data, *Geophys. J. Int.*, **173**(2), 382–394, doi: 10.1111/j.1365-246X.2008.03724.x.

Lesur, V., Wardinski, I., Asari, S., Minchev, B., & Mandea, M., 2010. Modelling the Earth's core magnetic field under flow constraints, *Earth, Planets and Space*, **62**, 503–516, doi: 10.5047/eps.2010.02.010.

Lesur, V., Rother, M., Vervelidou, F., Hamoudi, M., & Thébault, E., 2013. Post-processing scheme for modeling the lithospheric magnetic field, *Solid Earth*, **4**, 105–118, doi: 10.5194/sed-4-1345-2012.

Lesur, V., Whaler, K., & Wardinski, I., 2015. Are geomagnetic data consistent with stably stratified flow at the core-mantle boundary?, *Geophys. J. Int.*, **201**(2), 929 – 946, doi: 10.1093/gji/ggv031.

Lesur, V., Gillet, N., Hammer, M. D., & Mandea, M., 2022. Rapid variations of Earth's core magnetic field, *Surveys in Geophysics*, doi: 10.1007/s10712-021-09662-4.

Lühr, H. & Maus, S., 2010. Solar cycle dependence of quiet-time magnetospheric currents

and a model of their near-earth magnetic fields, *Earth Planets Space*, **62**(10), 843–848, doi: 10.5047/eps.2010.07.012.

Macmillan, S. & Olsen, N., 2013. Observatory data and the swarm mission, *Earth, Planets and Space*, **65**(11), 1355–1362, doi: 10.5047/eps.2013.07.011.

Maus, S. & Weidelt, P., 2004. Separating the magnetospheric disturbance magnetic field into external and transient internal contributions using a 1D conductivity model of the Earth, *Geophys. Res. Lett.*, **31**, L12614, doi: 10.1029/2004GL020232.

Olsen, N. & Mandea, M., 2008. Rapidly changing flows in the earths core, *Nature Geoscience*, **1**(6), 390–394, doi: 10.1038/ngeo203.

Olsen, N., Albini, G., Bouffard, J., Parrinello, T., & Tffner-Clausen, L., 2020. Magnetic observations from cryosat-2: calibration and processing of satellite platform magnetometer data, *Earth, Planets and Space*, **72**(1), 48, doi: 10.1186/s40623-020-01171-9.

Pais, M. & Jault, D., 2008. Quasi-geostrophic flows responsible for the secular variation of the earth's magnetic field, *Geophys. J. Int.*, **173**, 421–443, doi: 10.1111/j.1365-246X.2008.03741.x.

Pais, M. A., Morozova, A. L., & Schaeffer, N., 2015. Variability modes in core flows inverted from geomagnetic field models, *Geophys. J. Int.*, **200**, 402–420, doi: 10.1093/gji/ggu403.

Roberts, P. H. & Scott, S., 1965. On analysis of the secular variation, *Journal of geomagnetism and geoelectricity*, **17**(2), 137–151, doi: 10.5636/jgg.17.137.

Ropp, G., Lesur, V., Baerenzung, J., & Holschneider, M., 2020. Sequential modelling of the Earth's core magnetic field, *Earth, Planets and Space*, **72**(1), 153, doi: 10.1186/s40623-020-01230-1.

Thomson, A. & Lesur, V., 2007. An improved geomagnetic data selection algorithm for global geomagnetic field modelling, *Geophys. J. Int.*, **169**, 951–963, doi: 10.1111/j.1365-246X.2007.03354.x.

Tøffner-Clausen, L., Lesur, V., Olsen, N., & Finlay, C., 2016. In-flight scalar calibration and characterisation of the swarm magnetometry package, *Earth Planets and Space*, p. 68:129, doi: 10.1186/s40623-016-0501-6.

Whaler, K. A., 1980. Does the whole of the Earth's core convect?, *Nature*, **287**, 528–530, doi: 10.1038/287528a0.

APPENDIX A: NORMALISATION OF VECTOR SPHERICAL HARMONICS

Vector spherical harmonics are introduced in this manuscript in equation (3.1). The normalisation used has been described by Lesur & Vervelidou (2020). The $\hat{\mathbf{Y}}^m_{\ell,\ell+1}$ and $\hat{\mathbf{Y}}^m_{\ell,\ell-1}$ are defined by:

$$\begin{aligned}\hat{\mathbf{Y}}^m_{\ell,\ell+1}(\theta,\phi) &= -a\,(r/a)^{\ell+2}\,\nabla\left((a/r)^{\ell+1}\,Y^m_\ell(\theta,\phi)\right)\\ \hat{\mathbf{Y}}^m_{\ell,\ell-1}(\theta,\phi) &= -a\,(a/r)^{\ell-1}\,\nabla\left((r/a)^{\ell}\,Y^m_\ell(\theta,\phi)\right).\end{aligned} \tag{A.1}$$

The (θ,ϕ,r) are the usual colatitude, longitude and radius. a is a reference radius. The

$Y_\ell^m(\theta,\phi)$ are the Schmidt semi-normalized real spherical harmonics used in geomagnetism where negative orders, $m<0$, are associated with $\sin(|m|\phi)$ terms whereas null or positive orders, $m\geq 0$, are associated with $\cos(|m|\phi)$ terms. ∇ is the usual gradient operator. Although the radius r and the reference radius a appear in equations (A.1), the vector harmonics only depend on the colatitude and longitude. We use the normalisation:

$$\frac{1}{4\pi}\int_0^{2\pi}\int_0^{\pi}\hat{\mathbf{Y}}^m_{\ell,\ell'}(\theta,\phi)\hat{\mathbf{Y}}^m_{\ell,\ell''}(\theta,\phi)sin\theta\,d\theta\,d\phi=\begin{cases}\ell+1 & \text{if } \ell'=\ell''=\ell+1\\ \ell & \text{if } \ell'=\ell''=\ell-1\end{cases}. \tag{A.2}$$

The vector harmonics $\hat{\mathbf{Y}}^m_{\ell,\ell+1}$ and $\hat{\mathbf{Y}}^m_{\ell,\ell-1}$ are orthogonal for all values of ℓ – i.e.

$$\frac{1}{4\pi}\int_0^{2\pi}\int_0^{\pi}\hat{\mathbf{Y}}^m_{\ell,\ell+1}(\theta,\phi)\hat{\mathbf{Y}}^m_{\ell,\ell-1}(\theta,\phi)sin\theta\,d\theta\,d\phi=0. \tag{A.3}$$

APPENDIX B: ESTIMATION OF THE "RESOLVED" FLOW

The way the "resolved" flow is derived from the modelled flow is briefly described below.

As an output of the modelling process, each snapshot model of the core surface flow $\mathbf{m}$ comes with a posterior covariance matrix $\mathbf{C_m}$ that can be extracted from the full posterior covariance matrix of the model. This matrix $\mathbf{C_m}$ is symmetric real and definite positive. It can be decomposed as:

$$\mathbf{C_m}=\mathbf{V}\cdot\mathbf{L}\cdot\mathbf{V}^t \tag{B.1}$$

where $\mathbf{L}$ is a diagonal matrix which diagonal elements λ_i are the eigenvalues of $\mathbf{C_m}$. The matrix $\mathbf{V}$ is the matrix of the eigenvectors, and ^{t} indicates the transpose.

We introduced the vector $\mathbf{x}=\mathbf{V}^t\cdot\mathbf{m}$, that is the core surface flow model defined with the eigenvector basis. The eigenvalue λ_i is the variance of the element x_i of $\mathbf{x}$. A "resolved" model is set by defining a threshold for the signal to noise ratio $r_i=|x_i|/\sqrt{\lambda_i}$. For values of r_i under this threshold, the value of x_i is set to zero defining this way a vector $\tilde{\mathbf{x}}$. The "resolved" model in terms of spherical harmonic toroidal and poloidal components $\tilde{\mathbf{m}}$ is then reconstructed by:

$$\tilde{\mathbf{m}}=\mathbf{V}\cdot\tilde{\mathbf{x}} \tag{B.2}$$

In Figure (B1) is shown the number of ratio values r_i above different values of the threshold, as a function of time. We recall that a single snapshot has 2×728 degrees of freedom. Therefore the threshold values of 2, used in this work, considerably reduces the complexity of the flow model.

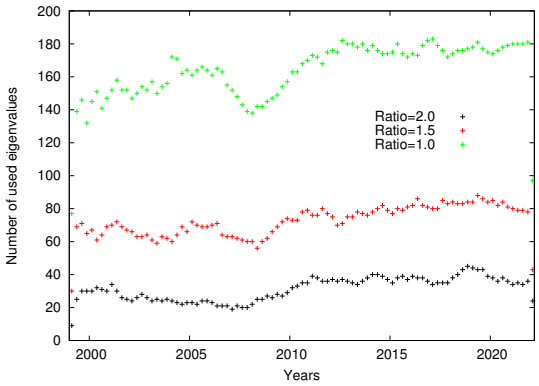

Figure B1. Number of ratio r_i above the threshold ratio = 2, 1.5 and 1, as a function of time.

APPENDIX C: FLOW PRINCIPAL COMPONENT ANALYSIS (PCA)

We describe briefly here how the principal component analysis was applied to the flow model. An example of principal component analysis application to core surface flow can also be found in Pais et al. (2015).

For each epoch t_k the toroidal and poloidal flow coefficients: $t^m_{\ell k}$, and $s^m_{\ell k}$, were set in a vector $\mathbf{h}_k$ following the canonical order:

$$\mathbf{h}_k = \left(t^0_{1k},\, t^1_{1k},\, t^{-1}_{1k},\, t^0_{2k}, \cdots, s^0_{1k},\, s^1_{1k},\, s^{-1}_{1k},\, s^0_{2k}, \cdots\right)^t. \tag{C.1}$$

The size of this vector is $1456 = 2 \times 728$ as the maximum spherical harmonic degree for the poloidal and toroidal flows is $\ell = 26$. There are 93 vectors $\mathbf{h}_k$, one for each epoch, that can be put together to build a matrix $\mathbf{H} = [\mathbf{h}_k]_{k=1,93}$. A singular value decomposition of the matrix $\mathbf{H}^t\mathbf{H}$ gives:

$$\mathbf{H}^t\mathbf{H} = \sum_{i=1}^{93} \lambda_i \mathbf{v}_i \mathbf{v}_i^t \tag{C.2}$$

where λ_i and $\mathbf{v}_i$, for $i = 1, \cdots, 93$, are the eigenvalues and eigenvectors of $\mathbf{H}^t\mathbf{H}$, respectively. Each of the eigenvectors is describing a typical behaviour in time that is associated with a flow pattern defined by a set of toroidal and poloidal flow coefficients given by the elements of the vector $\mathbf{u}_i$ with:

$$\mathbf{u}_i = \frac{1}{\sqrt{\lambda_i}} \mathbf{H} \cdot \mathbf{v}_i. \tag{C.3}$$

Each of the vector $\mathbf{u}_i$ defines a mode, with a temporal behaviour given by $\sqrt{\lambda_i}\mathbf{v}_i$. In Figure (9) we present the modes and temporal behaviours associated with the three largest eigenvalues.